

# Application of a Critical State Bounding Surface Model Implemented in Multilaminate Framework for Numerical Modeling of Soils

Hamid Karimpour  
Golder Associates Ltd., Calgary, Alberta, Canada  
Seyed Amiroding Sadrnejad  
Khaje-Nasir Toosi University of Technology, Tehran, Iran



Challenges from North to South  
Des défis du Nord au Sud

## ABSTRACT

A new plasticity model is proposed based on implementing a critical state based bounding surface model in multilaminate framework. The original bounding surface model is defined by the following four surfaces: (i) failure surface (ii) bounding surface; (iii) loading surface and (iv) plastic dilatancy surface. These surfaces are defined in multilaminate framework to introduce a new constitutive model. In this framework, the failure, bounding, loading and plasticity dilatancy surfaces are formulated on  $2 \times 13$  local planes with varying orientations over a virtual unit sphere around a stress point. A weight factor is assigned to each plane with respect to the volume of the unit sphere. The overall response of the material when subjected to a load will then be integrated by summation of the contributions of all planes. The model parameters are calibrated by modeling nine triaxial tests under different densities and confining stresses. Application of the new constitutive model is then studied by its implementation into a finite difference code and modeling a soil-pipe laboratory test. It is concluded that the new constitutive model could accurately predict the observed triaxial and laboratory tests.

## RÉSUMÉ

Un nouveau modèle de plasticité est proposé sur la base de la mise en œuvre d'un modèle multistratifié de surface englobante d'états critiques. Le modèle de surface de délimitation d'origine est défini par les quatre surfaces suivantes: (i) surface de rupture (ii) surface de délimitation; (iii) surface de chargement et (iv) surface plastique de dilatance. Ces surfaces sont définies dans le cadre du comportement multistratifié, afin d'introduire un nouveau modèle de comportement. Dans ce cadre, les surfaces de rupture, d'états limites, de chargement et de dilatance plastique sont formulées sur  $2 \times 13$  plans locaux avec des orientations variant sur une sphère unitaire virtuelle autour d'un point de contrainte. Un facteur de pondération est affecté à chaque plan par rapport au volume de la sphère unitaire. La réponse globale du matériau quand il est soumis à une charge est ensuite intégré par sommation des contributions de tous les plans. Les paramètres du modèle sont calibrés par la modélisation de neuf essais triaxiaux sous différentes densités et contraintes de confinement. L'application du nouveau modèle de comportement est ensuite étudiée par sa mise en œuvre dans un code en différences finies et par la modélisation d'un essai de laboratoire sol-canalisation. Il est conclu que le nouveau modèle de comportement pourrait prédire avec précision les essais triaxiaux et de laboratoire.

## 1 INTRODUCTION

A numerous number of constitutive models have been presented with different capabilities, mostly based on experimental observations of material behavior using elasticity and plasticity theories. Usefulness of these models will be based on various factors such as soil grading and texture, presence of water, loading condition, etc. To name a few, the following researchers have introduced classic constitutive models that have been widely used in geotechnical engineering: Drucker et al. (1957), Roscoe and Burland (1968), DiMaggio and Sandler (1971), Lade (1977), Prevost (1978), Mroz et al. (1981), Ghaboussi and Momen (1982), Desai and Faruque (1984), Poorooshasb and Pietruszak (1985), Dafalias and Herrmann (1986).

Taylor (1938) presented a framework referred to as multilaminate. Multilaminate framework is semi-micromechanical tool based on formulating a number of planes with varying orientations over a virtual unit sphere

around a stress point. A weight factor is assigned to each plane with respect to the volume of the unit sphere. The overall response of the material when subjected to a load will then be integrated by summation of the contributions of all planes.

Multilaminate framework is a tool and cannot predict the behavior of material independently. A constitutive law can be defined in this framework to take advantage of its features. By using this framework the overall behavior is, obtained by accumulating responses of the defined planes. Mathematically, any constitutive law could be used in this framework.

Batdorf and Budiansky (1949) presented a multilaminate plasticity theory for metals that considered development of plastic shear strain along the direction of the shear stress path component.

Zienkiewicz and Pande (1977) used Batdorf and Budiansky's constitutive model and expanded it to fractured rocks. A similar approach was also employed by Pande and Pietruszczak (1982) for prediction of

liquefaction of layered sand called reflecting surface model. In the same framework, Bazant and Oh (1983) presented a new model referred to as micro-plane for analyzing cracking in concrete. Pande and Pietruszczak (2001) provided a multilaminate model to describe soil anisotropy. Schweiger et al. (2009) provided a multilaminate model capable of considering both induced and inherent anisotropy for soils.

An existing bounding surface constitutive model, as proposed by Crouch et al. (1994) based on Dafalias and Herrmann (1986), is explained in the multilaminate framework to introduce a new constitutive model. In this article, a brief description of the new constitutive model is presented. Details of the new constructive model have been presented by Sadrnejad and Karimpour (2010). A series of available triaxial test results are used for showing the capability of the new model to predict the behavior of loose and dense sand specimens under a range of confining stresses.

This constitutive model is then used in a finite difference code to model a laboratory test that includes a pipe buried in sand under cyclic loading. Two laboratory tests are modeled and numerical and experimental results are compared.

## 2 UNIFIED BOUNDING SURFACE MODEL IN MULTILAMINATE FRAMEWORK

Using a multilaminate model, one could define a numerical relation between the microscopic and macroscopic behaviours. An existing bounding surface constitutive model, as proposed by Crouch et al. (1994) and referred to as unified critical state bounding model has been defined in the multilaminate framework.

The original bounding surface constitutive model uses two different radial and deviatoric mapping rules to define the loading surface based on the failure surface. Also, an innovative approach, based on movement of the mapping center are used in this model to observe the rotation of the principal stress axes and account for imposed anisotropy effects. The intrinsic anisotropy and bedding effects can be considered when using the multilaminate model by defining different material parameters on different planes.

### 2.1 Definition of Planes and Local Coordinates

To satisfy conditions of the multilaminate framework from the engineering viewpoint and reduce high computational costs, a limited number of sampling planes are used. Considering a good distribution of plastic deformation and avoiding high computing time, the choice of 13 independent planes as shown in Figure 1 is a fair number for solution of any three dimensional problem.

The components of the unit normal vector of plane  $i$  ( $l_i$ ,  $m_i$  and  $n_i$ ) and plane's weight coefficients ( $w_i$ ) for the numerical integration rule are presented in Table 1. The coefficients  $w_i$  have been calculated based on Gauss Quadrature numerical integration rule. The presented  $w_i$  are acceptable for a first order tensor and are corrected for a second order tensor like (e.g., stress or strain) by multiplying the ratio of area for each plane on the unit sphere.

A coordinate system has been used for each plane such that one axis is perpendicular to the plane and two axes are on the plane. Plastic shear strains are considered on the planes.

Table 1. Plane's unit vector components and weight coefficients for numerical integration.

Plane		1	2	3	4	5	6	7	8	9	10	11	12	13
Normal Axis	$l_i$	$\frac{\sqrt{3}}{3}$	$\frac{\sqrt{3}}{3}$	$-\frac{\sqrt{3}}{3}$	$-\frac{\sqrt{3}}{3}$	$\frac{\sqrt{2}}{2}$	$-\frac{\sqrt{2}}{2}$	$\frac{\sqrt{2}}{2}$	$-\frac{\sqrt{2}}{2}$	0	0	1	0	0
	$m_i$	$\frac{\sqrt{3}}{3}$	$-\frac{\sqrt{3}}{3}$	$\frac{\sqrt{3}}{3}$	$-\frac{\sqrt{3}}{3}$	$\frac{\sqrt{2}}{2}$	$\frac{\sqrt{2}}{2}$	0	0	$-\frac{\sqrt{2}}{2}$	$\frac{\sqrt{2}}{2}$	0	1	0
	$n_i$	$\frac{\sqrt{3}}{3}$	$\frac{\sqrt{3}}{3}$	$\frac{\sqrt{3}}{3}$	$\frac{\sqrt{3}}{3}$	0	0	$\frac{\sqrt{2}}{2}$	$\frac{\sqrt{2}}{2}$	$\frac{\sqrt{2}}{2}$	$\frac{\sqrt{2}}{2}$	0	0	1
$w_i$		$\frac{27}{840}$	$\frac{27}{840}$	$\frac{27}{840}$	$\frac{27}{840}$	$\frac{32}{840}$	$\frac{32}{840}$	$\frac{32}{840}$	$\frac{32}{840}$	$\frac{32}{840}$	$\frac{32}{840}$	$\frac{40}{840}$	$\frac{40}{840}$	$\frac{40}{840}$

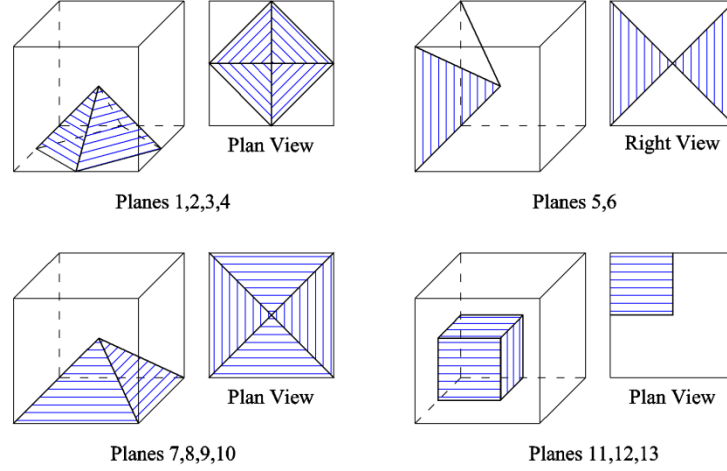


Figure 1. Planes used in the presented multilaminate constitutive model.

## 2.2 Stress and Strain Vectors

In the following equations  $\{ \}$  and  $[ ]$  denote a 9-element vector and a 3 by 3 matrix, respectively. Superscript T indicates a transposed array. A superposed dot indicates the rate and  $| \cdot |$  refers to the norm. Following this notation  $\| \{ \} \|$  is the length of a vector whereas  $\{ \cdot \}$  represents a unit vector ( $\{ \cdot \} = \{ \cdot \} / \| \{ \cdot \} \|$ ). A comma followed by a subscripted variable implies the partial derivative with respect to that variable. Bars over the stress quantities refer to points on the bounding surface. The effective stress, strain and Kronecker's delta vectors are defined as follows:

$$\begin{aligned} \{\varepsilon\} &= \{\varepsilon_{11} \quad \varepsilon_{22} \quad \varepsilon_{33} \quad \varepsilon_{12} \quad \varepsilon_{21} \quad \varepsilon_{13} \quad \varepsilon_{31} \quad \varepsilon_{23} \quad \varepsilon_{32}\}^T \\ \{\sigma\} &= \{\sigma_{11} \quad \sigma_{22} \quad \sigma_{33} \quad \sigma_{12} \quad \sigma_{21} \quad \sigma_{13} \quad \sigma_{31} \quad \sigma_{23} \quad \sigma_{32}\}^T \\ \{\delta\} &= \{1 \quad 1 \quad 1 \quad 0 \quad 0 \quad 0 \quad 0 \quad 0 \quad 0\}^T \end{aligned} \quad (1)$$

The applied stress vector is proportioned to each plane by multiplying related transitive matrix  $[T_i]$  that are derived from the unit vectors. The following stress components are defined on each plane:

$$\begin{Bmatrix} \tau_1 \\ \tau_2 \\ \sigma_n \end{Bmatrix}_i = [T_i] \cdot \{\sigma\}, \quad \tau = \sqrt{\tau_1^2 + \tau_2^2} \quad (2)$$

where  $[T_i]$  is defined as:

$$[T_i] = \begin{bmatrix} L_{x'x} & L_{x'y} & L_{x'z} \\ L_{y'x} & L_{y'y} & L_{y'z} \\ L_{z'x} & L_{z'y} & L_{z'z} \end{bmatrix} \cdot \begin{bmatrix} l_i & 0 & 0 & m_i & 0 & n_i & 0 & 0 & 0 \\ 0 & m_i & 0 & 0 & l_i & 0 & 0 & n_i & 0 \\ 0 & 0 & n_i & 0 & 0 & 0 & l_i & 0 & m_i \end{bmatrix} \quad (3)$$

The stress ratio of each plane is defined as follows:

$$\zeta = \frac{\tau}{\sigma_n} \quad (4)$$

## 2.3 Plasticity of New Constitutive Model

The plasticity of the new model is generally similar to the original model as proposed by Crouch et al. (1994) and follows the classic plasticity:

$$\{\dot{\varepsilon}\} = \{\dot{\varepsilon}^e\} + \{\dot{\varepsilon}^p\} \quad (5)$$

which states separate components of elastic  $\{\dot{\varepsilon}^e\}$  and plastic  $\{\dot{\varepsilon}^p\}$  strain vectors:

$$\begin{aligned} \{\dot{\varepsilon}\} &= [C^e]_T \cdot \{\dot{\sigma}\} + [C^p]_T \cdot \{\dot{\sigma}\} \\ [C^{ep}]_T &= [C^e]_T + [C^p]_T \end{aligned} \quad (6)$$

where  $[C^e]$  and  $[C^p]$  are defined for each plane as:

$$\begin{aligned} [C^e]_i &= \frac{1}{2G_i} [I] + \left( \frac{1}{9K_i} - \frac{1}{6G_i} \right) \cdot \{\delta\} \cdot \{\delta\}^T \\ [C^p]_i &= \frac{1}{H_i} \{Q\}_i \cdot \{P\}_i^T \end{aligned} \quad (7)$$

where,  $K_i$  and  $G_i$  are bulk and shear moduli at plane  $i$ .  $\{Q\}$  and  $\{P\}$  are defined as the unit normal to the loading surface and the unit direction of the plastic strain rate, respectively.  $[C^e]_T$  and  $[C^p]_T$  are calculated based on numerical integration as follows:

$$\begin{aligned} [C^p]_T &= 8\pi \cdot \sum_{i=1}^{13} w_i \cdot [C^p]_i \\ [C^e]_T &= 8\pi \cdot \sum_{i=1}^{13} w_i \cdot [C^e]_i \end{aligned} \quad (8)$$

The following 4 surfaces must be defined in this constitutive model:

- Failure surface to describe the critical state;
- Bounding surface to record the previous loading dominion and defining the plastic loading surface;

- Loading surface to define the direction of plastic loading; and,
- Plastic dilatancy surface, which is determined using the ratio of volumetric to deviatoric plastic strain.

Details of the original and the new multilaminate models are presented by Crouch et al. (1994), and Sadrnejad and Karimpour (2010). A brief description of the new model is presented herein.

## 2.4 Failure Surface

For simplicity, in the multilaminate model failure surface is assumed as Mohr-Coulomb form instead of the original elliptic form. This surface is specified by critical effective stress ratio,  $\zeta_{cr}$ . The critical state is shown in Figure 2.

## 2.5 Bounding Surface

The boundary surface is a three-sector surface constructed with (i) a compressive ellipse, (ii) a hyperbola and (iii) a tensile ellipse as shown in Figure 2. The compressive elliptic part lies in  $\sigma_{n_1} \leq \sigma_n \leq \sigma_{n_0}$  region where  $\sigma_{n_1} = \sigma_{n_0}/R$ .  $R$  is a material constant ( $1 \leq R < \infty$ ).  $\sigma_{n_0}$  varies as a function of the volumetric plastic strain and defines the size of bounding surface. The compressive ellipse meets the normal stress axis perpendicularly. The equation of the compressive ellipse is given as:

$$F = \bar{\tau} - \frac{N \cdot \sigma_{n_0}}{R} \sqrt{1 - \left( \frac{R\bar{\sigma}_n/\sigma_{n_0} - 1}{R-1} \right)^2} = 0 \quad (9)$$

$N$  is the slope of a line passing from stress origin to the common tangent point of ellipse and hyperbola sectors. The hyperbola is located in  $0 < \sigma_n < \sigma_{n_1}$  region and defined as:

$$F = \bar{\tau} - \frac{N \cdot \sigma_{n_0}}{R} \left( 1 + \frac{AR}{N} - \sqrt{\left( 1 - \frac{R\bar{\sigma}_n}{\sigma_{n_0}} \right)^2 + \left( \frac{AR}{N} \right)^2} \right) = 0 \quad (10)$$

The gap between N-line and the asymptote to the hyperbolic sector is controlled by  $A \cdot \sigma_{n_0}$ . The last sector is a tensile ellipse situated in  $\sigma_{n_3} \leq \sigma_n \leq 0$  region and is defined as:

$$F = \bar{\tau} - \tau_r \sqrt{1 - \left( 1 - \frac{\bar{\sigma}_n - T\sigma_{n_0}}{\sigma_{n_r}} \right)^2} = 0 \quad (11)$$

$$\sigma_{n_r} = \frac{\sigma_{n_0} \cdot T^2 \cdot (\Psi/\tau_2)}{1 + 2\sigma_{n_0} \cdot T \cdot (\Psi/\tau_2)} \quad (12)$$

$$\tau_r = \tau_2 / \sqrt{1 - \left( 1 + (T\sigma_{n_0}/\sigma_{n_r}) \right)^2} \quad (13)$$

$$\Psi = \frac{N}{\sqrt{1 + (AR/N)^2}} \quad (14)$$

$$J_2 = \frac{N \cdot \sigma_{n_0}}{R} \left( 1 + \frac{AR}{N} - \sqrt{1 + (AR/N)^2} \right) \quad (15)$$

## 2.6 Loading Surface

The stress point is always located on the loading surface that is defined based on the bounding surface using radial scaling method in the compressive elliptic sector ( $\sigma_n > \sigma_{n_0}/R$ ) and deviatoric scaling method elsewhere ( $\sigma_n \leq \sigma_{n_0}/R$ ).

$\beta$  is defined as the scaling coefficient and defined as:

$$\beta = \frac{\bar{\tau}}{\tau} \quad (16)$$

However, in the case of isotropic loading (stress point on the  $\sigma_n$  axis) the it can be calculated as:

$$\beta = (\sigma_{n_0} \cdot (1/R - 1)) / (\sigma_{n_0}/R - \sigma_n) \quad (17)$$

The loading surface equation in the radial scaling region is defined by substituting  $(\sigma_{n_0}/R) + \beta(\sigma_n - (\sigma_{n_0}/R))$  for  $\bar{\sigma}_n$  and  $\beta\tau$  for  $\bar{\tau}$  in the compressive sector of the bounding surface (Equation 9):

$$f = \beta\tau - \frac{N \cdot \sigma_{n_0}}{R} \sqrt{1 - \left( \frac{\beta(R\sigma_n/\sigma_{n_0} - 1)}{R-1} \right)^2} = 0 \quad (18)$$

The other two sectors of the loading surface will simply be defined by replacing  $\bar{\sigma}_n$  by  $\sigma_n$  for and  $\bar{\tau}$  by  $\beta\tau$  in Equations 10 and 11:

$$f = \beta\tau - \frac{N \cdot \sigma_{n_0}}{R} \left( 1 + \frac{AR}{N} - \sqrt{\left( 1 - \frac{R\sigma_n}{\sigma_{n_0}} \right)^2 + \left( \frac{AR}{N} \right)^2} \right) = 0 \quad (19)$$

$$f = \beta\tau - \tau_r \sqrt{1 - \left( 1 - \frac{\sigma_n - T\sigma_{n_0}}{\sigma_{n_r}} \right)^2} = 0 \quad (20)$$

The direction of plastic loading vector could be obtained from the following equation:

$$\{Q\} = \frac{1}{\| \{f, \sigma\} \|} \cdot \left( \underbrace{f, \sigma}_{\text{hydrostatic}} \cdot \{ \sigma_n, \sigma \} + \underbrace{f, \tau}_{\text{deviatoric}} \cdot \{ \tau_r, \sigma \} \right) \quad (21)$$

## 2.7 Plastic Dilatancy Surface and Plastic Strain Direction

Similar to the loading surface, plastic dilatancy surface is also passing through the stress point and geometrically

similar to bounding surface; however, a different scaling method is used to define the plastic dilatancy surface from the bounding surface. In addition, there is dissimilarity in comparison to bounding surface regarding the compressive ellipse sector. The power of two in Equation (9) is changed to  $n_g$ ; thus, for  $2 < n_g < \infty$  we have super-ellipse and for  $1 < n_g < 2$  there is a sub-ellipse:

$$g = \tau - \frac{N_g \cdot \sigma_{n_0 g}}{R_g} \cdot \left( 1 - \left( \frac{(R_g \sigma_n / \sigma_{n_0 g} - 1)^{n_g}}{R_g - 1} \right)^{\frac{1}{n_g}} \right) = 0 \quad (22)$$

Despite of the fact that the bounding and plastic dilatancy surfaces are geometrically identical, the non-associated flow rule exists as the direction of loading increment vector differs from the direction of the plastic strain increment vector. The direction of plastic strain vector can be evaluated as:

$$\{P\} = \frac{1}{\{g, \sigma\}} \cdot \left( g, \sigma_n \cdot \{\sigma_n, \sigma\} + f, \tau \cdot \{\tau, \sigma\} \right) \quad (23)$$

The surfaces described above are schematically shown in Figure 2.

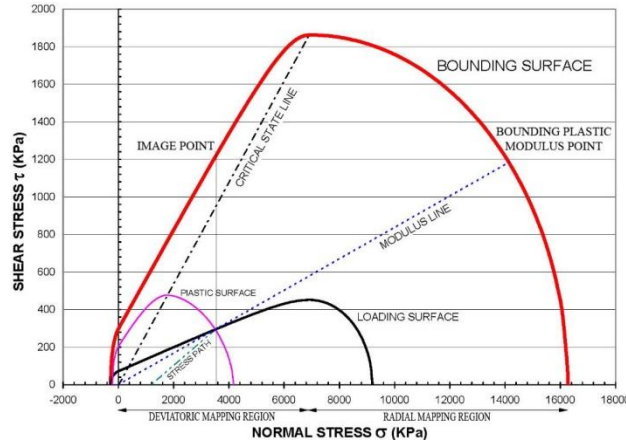


Figure 2. Schematic presentation of the different surfaces in bounding surface model.

A full description of hardening/softening and dependency of the bulk modulus on the stress state (hyper elastic formulation) has been presented by Sadrnejad and Karimpour (2010) and has not been discussed herein.

### 3 VERIFICATION OF THE NEW MULTILAMINATE MODEL

Results of nine drained triaxial tests performed on sand in two different densities were chosen to verify the predictions of the new multilaminate model. Figure 3 compares the stress-strain and volumetric behavior for loose sand specimens ( $e_{in}=0.86$ ) under a four confining stresses,  $\sigma_3$ . The specimen sheared under the highest

confining stress undergoes contraction at all times during testing, while sample under the lowest confining stress shows minor contraction for axial strain up to approximately 2% and experiences dilation afterwards.

Figure 4 shows the laboratory and numerical results for five dense specimens ( $e_{in}=0.60$ ). As expected, significant dilation is observed for the specimen sheared under the lowest confining stress. However, the specimen sheared under the highest confining experiences minor volume change.

Comparison of the numerical and laboratory results presented in Figures 3 and 4 indicates that the new multilaminate model is capable of capturing the behavior of loose and dense sand specimens under low and high confining stresses.

In the next sections, the capability of the new multilaminate model is assessed by its implementation into a finite difference code and comparison of the numerical and laboratory results of a soil-pile experiment.

The process of the calibration of the material parameters input to the new multilaminate model is not discussed here in.

An extensive discussion on the input material parameters to the new multilaminate model and their impact on the stress-strain and volumetric behaviors have been presented by Sadrnejad and Karimpour (2010).

### 4 IMPLEMENTATION OF NEW CONSTITUTIVE MODEL IN A FINITE DIFFERENCE CODE

The new multilaminate model was incorporated into a finite-difference code (FLAC 5.0) that is capable of numerical modeling of soils, rocks and similar materials. This code is based on Lagrangian calculations and it has an appropriate structure to model large strains.

The individual-point code of the new multilaminate model was first written and checked. The model was then written in C++ program and exported as a Dynamic Link Library (DLL) file to be implemented in the finite difference code as a User Defined Model (UMD). This code was used to numerically model a soil-pipe experiment.

## 5 LABORATORY TESTS

### 5.1 Experimental Setup

A series of laboratory tests were performed on small diameter HDPE pipes buried in sand under repeated loading by Tafreshi and Khalaj (2008) who used a tank that included two soil types and was 220 mm long, 1000 mm wide and 1000 mm deep.

The Type I soil was uniform medium sand used in a range of densities and expressed as a trench soil to cover a buried 110 mm HDPE pipe. The Type II soil was used as the external medium of the experiment including the trench walls. Mechanical properties of two soil types are presented in Table 2

Table 2. Mechanical properties of soils used in laboratory tests.

Laboratory Test	Type I	Soil Type II
Particle Size Distribution (ASTM D422)	$C_u=1.51$ $C_c=1.29$ $D_{60} = 0.65$ mm $D_{30} = 0.60$ mm $D_{10} = 0.43$ mm	$C_u=13.75$ $C_c=0.79$ $D_{60} = 4.85$ mm $D_{30} = 1.17$ mm $D_{10} = 0.35$ mm
Specific Gravity (ASTM D854)	$G_s = 2.67$	-
Minimum Index Density and Unit Weight (ASTM D4254)	$e_{min} = 1.12$ $\rho_{d max} = 1.26$ gr/cm <sup>3</sup>	-
Maximum Index Density and Unit Weight (ASTM D4253)	$e_{min} = 0.55$ $\rho_{d max} = 1.72$ gr/cm <sup>3</sup>	-
Modified Proctor Maximum Dry Density	-	$\rho_{d max} = 2.30$ gr/cm <sup>3</sup> $W_{opt} = 6.6\%$

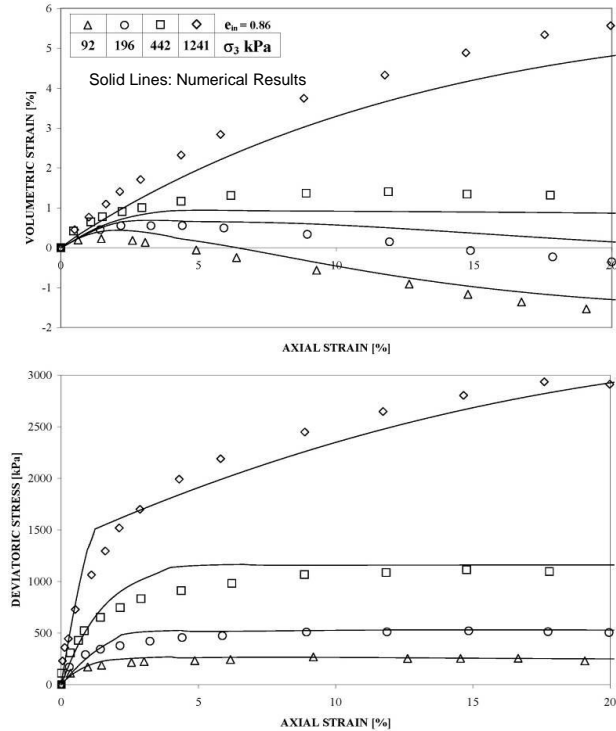


Figure 3. Axial strain versus deviatoric stress and volumetric strain in the loose sand ( $e=0.86$ ).

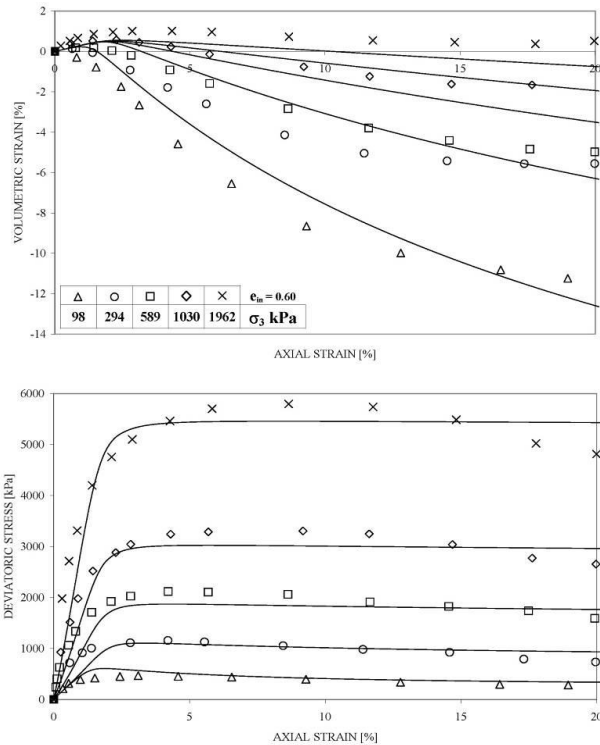


Figure 4. Axial strain versus deviatoric stress and volumetric strain in the Dense sand ( $e=0.60$ ).

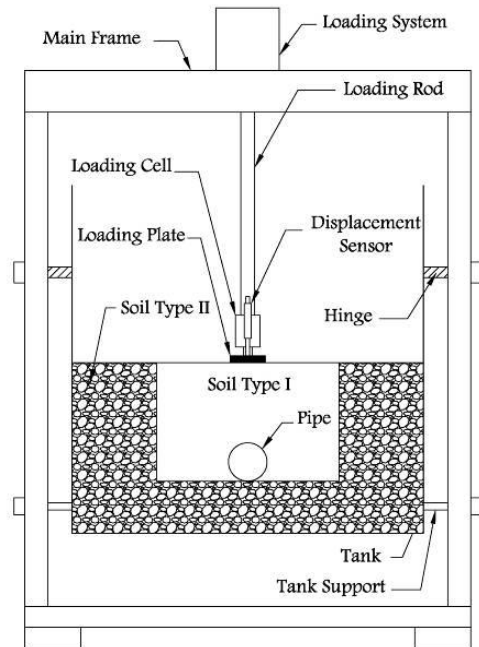


Figure 5. Schematic view of the experiment tank and soil trench

Figure 5 schematically shows the experimental setup that included a radius displacement transducer, a load cell and a linear variable differential transducer (LVDT). A dry pluviation device with different pluviation heights was used to reach the desired density of the Type I soil.

## 5.2 Selected Laboratory Tests

Three tests were selected to verify capability of the new multilaminate model in this paper. The first two tests had been performed without a buried pipe considering relative dry densities of 57% and 72% for Type I soil.

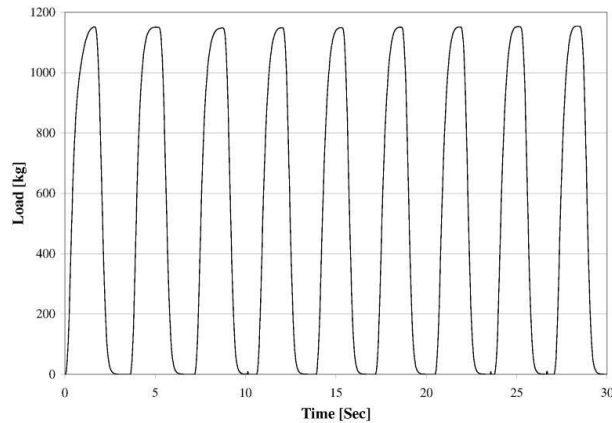


Figure 6. Loading pattern (stress of 5.5 kg/cm<sup>2</sup>) through the time

The third test included a pipe located at center depth of approximately 220 mm (2 pipe diameters) and relative dry density of 57%. Note that the trench width was 500 mm and constant for all three tests. A typical applied loading pattern is shown in Figure 6 for a maximum applied stress of 5.5 kg/cm<sup>2</sup>. Table 3 summarises the details of the laboratory tests selected for numerical modeling.

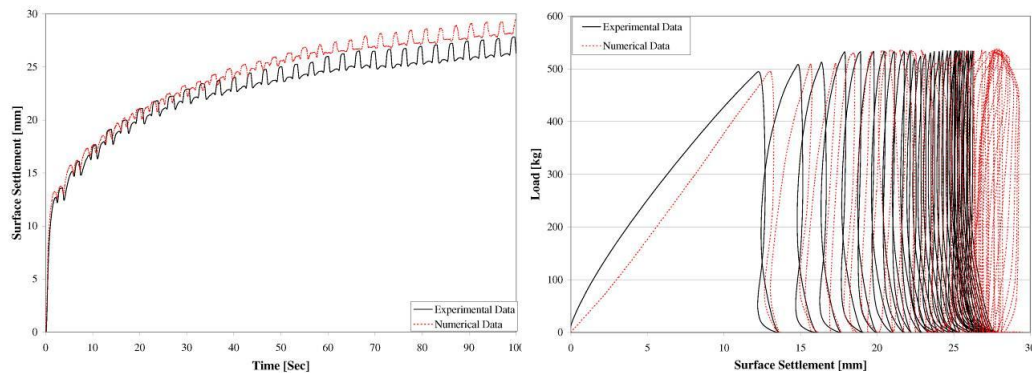


Figure 8. Settlement-time and settlement-load for relative density of 57% and applied stress of 2.5 kg/cm<sup>2</sup>.

Table 3. Summary of laboratory tests selected for numerical modeling

Experiment	Soil Type I Relative Dry Density (%)	Pipe Depth (mm)	Maximum Applied Stress (kg/cm <sup>2</sup> )
1	57%	-	2.5
2	72%	-	5.5
3	57%	220	2.5

## 6 COMPARISON OF RESULTS OF NUMERICAL ANALYSIS AND LABORATORY TEST

The comparison of the numerical analysis and laboratory results are presented in Figure 7 to Figure 10.

The measured settlement and load with respect to time for the first and second tests without a buried pipe are shown in Figures 7 and 8, respectively. The average difference between the measured and predicted settlement for the first and second tests are 2% and 3% respectively.

In the third test, a buried pipe is present and the radial deformation is measured. Figure 9 presents the measured settlement versus time and the applied load. The measured radial deformation versus time and the applied load in Figure 10. The average difference between the measured and predicted plate settlement and pipe radial deformation are 12% and 16%, respectively.

As observed, presence of the buried pipe resulted in an increase of the measured and predicted deformations. This is partially due to soil-pipe interaction. In general, there is a good agreement between the results of the numerical analysis and laboratory tests indicating the capability of the new multilaminate model in predicting the soil behavior under repeated loading

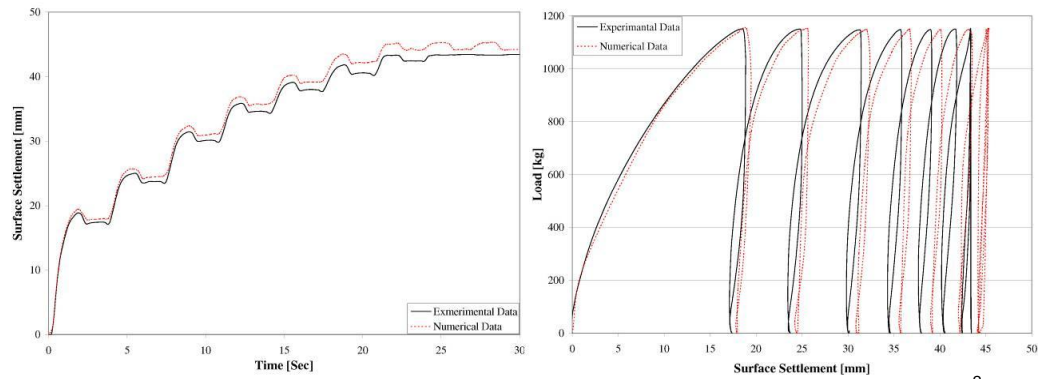


Figure 7. Settlement-time and settlement-load for relative density of 72% and applied stress of 5.5 kg/cm<sup>2</sup>.

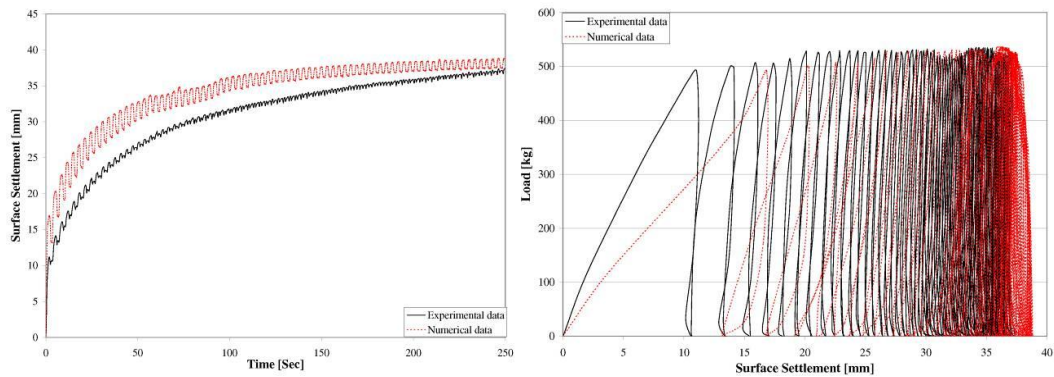


Figure 9. Settlement-time and Settlement-load for relative density of 57%, burial depth of 220 mm and applied stress of 2.5 kg/cm<sup>2</sup>.

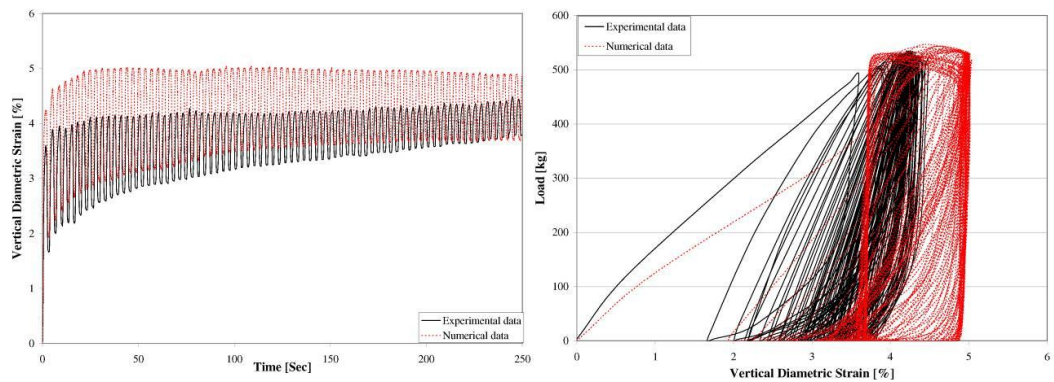


Figure 10. Vertical diametric strain-time and vertical diametric-load for relative density of 57%, burial depth of 220 mm and applied stress of 2.5 kg/cm<sup>2</sup>.

#### ACKNOWLEDGEMENTS

The writers would like to acknowledge Dr. Omid Khalaj for providing the laboratory test results.

#### REFERENCES

Drucker, D.C., Gibson, R.E., and Henkel, D.I. 1957. Soil mechanics and work-hardening theories of plasticity. *Trans., ASCE*, 122, 338-346.

Roscoe, K.H., and Burland, J.B. 1968. On the generalized stress-strain behaviour of 'wet' clay. *Engineering Plasticity*. J. Heymann and F. A. Leckie, eds., Cambridge University Press, Cambridge, England, 535-609.

DiMaggio, F.L. and Sandler, I.S. 1971. Material model for granular soils. *Journal of Engineering Mechanics Div., ASCE*, 97 (3), 935-950.

Lade, P.V. 1977. Elasto-plastic stress-strain theory for cohesionless soil with curved yield surfaces. *International Journal of Solids Structure*, 13, 1019-1035.

- Prevost, J-U. 1978. Plasticity theory for soil stress-strain behavior. *Journal of Engineering Mechanics Div., ASCE*, 104 (5), 1177-1194.
- Mroz, Z., Norris, V.A., and Zienkiewicz, O.C. 1981. An anisotropic, critical state model for soils subjects to cyclic loading. *Geotechnique*, London, England, 31 (4), 451-469.
- Ghaboussi, J. and Momen, H., 1982. Modeling and analysis of cyclic behavior of sands, G. N. Pande and O. C. Zienkiewicz (eds), *Soil Mechanics-Transient and Cyclic Loads*, Wiley, New York, 313-342.
- Desai, C.S., and Faruque, M.O. 1984. Constitutive model for (geological) materials.' *Journal of Engineering Mechanics*, ASCE, 110 (9), 1391-1408.
- Poorooshasb, H.B. and Pietruszczak, S. 1985. On yielding and flow of sand; a generalized two-surface model, *Computers and Geomechanics*, 1, 33-58.
- Dafalias, Y.F. and Herrmann, L.R. 1986. Bounding surface plasticity. II: Application to isotropic cohesive soils, *Journal of Engineering Mechanics*, 112 (12), 1263-1291.
- Frantziskonis, G., Desai, C.S., and Somasundaram, S. 1986. Constitutive model for non-associative behavior. *Journal of Engineering Mechanics*, ASCE, 112 (9), 932-946.
- Crouch, R.S. and Wolf, J.P. 1994. Unified 3D Critical State Bounding Surface Plasticity Model for Soils Incorporating Continuous Plastic Loading under Cyclic Paths. Part I: Constitutive relations, *International Journal of Numerical and Analytical Methods in Geomechanics*, 18, 735-758.
- Taylor G.I. 1938. Plastic strain in metals. *Journal of Industrial Metals*, 62, 307-324.
- Batdorf S.B. and Budiansky B. 1949. A mathematical theory of plasticity based on the concept of slip. National advisory committee for Aeronautics, T1871.
- Zienkiewicz, O.C., Pande G.N. 1977. Time-dependent Multilaminate model of rocks - a numerical study of deformation and failure of rock masses, *International Journal of Numerical and Analytical Methods in Geomechanics*, 1 (3), 219-247.
- Pande G.N. and Pietruszczak S. 1982. Reflecting surface model for soils, proceeding International Symposium Numerical Methods in Geomechanics, Zurich, A.A. Balkema, Rotterdam, 50-64.
- Pande G.N. and Sharma K.G. 1983. Multilaminate model of clays, *International Journal of Numerical and Analytical Methods in Geomechanics*, 7 (4), 397-418.
- Bazant Z.P. and Oh B.H. 1983. Micro plane model for fracture analysis of concrete structures, Proceeding Symposium on the interaction of Non-nuclear munitions with structures, published by McGregor & Werner, Washington.
- Pietruszczak S. and Pande G.N. 2001. Description of soil anisotropy based on multi-laminate framework. *Int. journal for numerical and analytical methods in geomechanics*. Vol. 25, pp 197-206
- Sadrnejad S.A., Karimpour H. 2010. A Bounding Surface Model for Sand Behaviour under Drained and Undrained Conditions, *International Journal of Civil Engineering* 9 (2), 96-110.
- Schweiger, H.F., Wiltafsky, C., Scharinger, F. and Galavi, V. 2009. A multilaminate framework for modelling induced and inherent anisotropy of soils. *Geotechnique* 59 (2), 87-101.